

Observing Kinematic Anisotropies of the Stochastic Background with LISA

Lavinia Heisenberg,^{1,*} Henri Inchauspé,^{1,†} and David Maibach^{1,‡}

¹*Institute for Theoretical Physics, University of Heidelberg, Philosophenweg 16 D-69120 Heidelberg Germany*

(Dated: January 29, 2024)

We propose a diagnostic tool for future analyses of stochastic gravitational wave background signals of extra-galactic origin in LISA data. Next-generation gravitational wave detectors hold the capability to track unresolved gravitational waves bundled into a stochastic background. This composite background contains cosmological and astrophysical contributions, the exploration of which offers promising avenues for groundbreaking new insights into very early universe cosmology as well as late-time structure formation. In this article, we develop a full end-to-end pipeline for the extraction of extra-galactic signals, based on kinematic anisotropies arising from the galactic motion, via full-time-domain simulations of LISA's response to the gravitational wave anisotropic sky. Employing a Markov-Chain-Monte-Carlo map-making scheme, multipoles up to $\ell = 2$ are recovered for scale-free spectra that support an interpretation as signals originating from cosmic strings in the case of a high signal-to-noise ratio. We demonstrate that our analysis is consistently beating cosmic variance and is robust against statistical and systematic errors. The impact of instrumental noise on the extraction of kinematic anisotropies is investigated, and we establish a detection threshold of $\Omega_{GW} \gtrsim 5 \times 10^{-8}$ in the presence of instrument-induced noise. Potential avenues for improvement in our methodology are highlighted.

I. INTRODUCTION

The continuous enhancement of Gravitational Wave (GW) measurements has ushered in a new era in GW astronomy. While the initial detection efforts focused on resolved waveforms, such as the first measurement by the LIGO/Virgo collaboration in 2015 [1], we are now approaching the capability of detecting unresolved GW sources with upcoming probes [2–4]. The sheer number of unresolved sources is so vast that they collectively create a stochastic signal known as the Stochastic Gravitational Waves Background (SGWB). This background encompasses a wide array of contributions from astrophysical as well as cosmological sources (see [4] and related references for a comprehensive review). Rich in its phenomenology, the SGWB can serve as compelling evidence for new physics on cosmological scales, offering a distinct avenue of exploration beyond high-energy physics at the TeV scale and probing the early universe prior to the Cosmic Microwave Background (CMB). Very recently, Pulsar Timing Arrays (PTAs) [5] have managed to collect initial evidence of a stochastic background [6, 7] flooding the universe. Despite the origins of this background remaining uncertain to this day, the results of PTA represents the initial step in identifying the astrophysical contributions to the SGWB. With forthcoming space-based instruments like the the Laser Interferometer Space Antenna (LISA) [8], insights gained from PTA can be supported by additional data potentially enhancing the current upper limits on the SGWB from ground-based instruments [9–11]. In addition, future ground-based instruments, such as the Einstein Tele-

scope [12, 13] and Cosmic Explorer [14, 15], will play a pivotal role in extending the frequency range over which both resolved and unresolved GW sources can be detected. Jointly, space- and ground-based instruments possess the potential to guide prospective detection efforts regarding the SGWB, offering exciting prospects for future GW research.

Due to its rich phenomenology, the cosmological component within the SGWB represents a smoking gun for new physics. However, a direct detection of such poses a substantial difficulty for data analysts: The SGWB is predominantly shaped by astrophysical sources, including white dwarf binaries, stellar mass black hole inspirals, and extra-galactic mergers, which augment the diverse range of primordial features in the spectrum. The task of distinguishing between the instrumental noise, the galactic and the extra-galactic (incl. cosmological) components of the stochastic imprint, without spoiling either of the components, remains one of the major challenges and priorities in the field of SGWB measurements [2, 16, 17]. A valuable tool in the complex task of disentangling distinct sources within the SGWB is to leverage observer-dependent features that can enhance the detectability against undesirable foreground confusion and instrumental noise. One of the prominent observer-dependent effects within the SGWB is characterized by kinematic features arising from the inherent motion of our local group of galaxies [18–21]. While galactic sources remain unaffected, the (ground- and space-based) detectors' motion with respect to the rest frame of primordial stochastic GW sources introduces Doppler anisotropies for primordial contributions to the SGWB only. As a result, we anticipate a Doppler-induced increase of power in lower-order multipole patterns of cosmological contributions within the SGWB, similar to what has been found in the CMB many decades ago. Thus, the analysis of kinematic anisotropies in the SGWB holds considerable promise

* heisenberg@thphys.uni-heidelberg.de

† h.inchauspe@thphys.uni-heidelberg.de

‡ d.maibach@thphys.uni-heidelberg.de

and has already generated substantial interest within the scientific community [2, 20, 22–24].

In this work, we aim to build upon previous investigations and build a diagnostic map-making scheme to be employed primarily (but not exclusively) in the hunt for the extra-galactic sources within SGWB data captured by LISA. Our study presents a full time-domain (4 years) simulation of GW anisotropic sky via the LISA Simulation Suite (LISAGWResponse [25, 26], LISAINstrument [27, 28]) and post-processing software (PyTDI [29]) needed to perform the Time Delay Interferometry (TDI) combination of the optical measurements and compose the final interferometer observables [30]. We utilize a map-making strategy based on a Monte-Carlo Markov Chains (MCMC) scheme, instead of the commonly used Fisher analysis, to investigate the detectability of kinematic anisotropies in simulated SGWB data (see [31] for similar investigations regarding background from galactic sources).

This article is structured as follows: In section II we review how Doppler-induced anisotropies manifest in the angular mode decomposition of the energy density spectrum $\Omega_{GW}(f, \hat{\mathbf{k}})$ of a given source. As for the potential seeds for the tested $\Omega_{GW}(f, \hat{\mathbf{k}})$, we present three models that are actively discussed in literature and can be associated to physical models of significant phenomenological importance. We elaborate on how anisotropic sky data is processed by LISA, including a description of the response function in section III. We start by summarizing the data generation procedure in III D. Subsequently, based on the simulated interferometer (4-years long) time series data-streams, we present our map-making strategy and the applied MCMC scheme in sections IV A and IV B respectively, aiming at recovering the injected intensity map. Here, we outline different approaches to recover the lower multipoles from a map reconstructed from LISA data. Finally, we present the result of our simulations for selected SGWB features and compare them with respect to their performance with the inclusion of instrumental noise in V. In section VI, we close our discussion with concluding remarks and an outlook into future work, discussing in particular the improvement of performance of the here presented pipeline in the presences of more complex spectral features.

II. DOPPLER-BOOSTED ANISOTROPIES AS SMOKING-GUN FOR EXTRA-GALACTIC ORIGIN

We initiate this investigation by briefly outlining the fundamental aspects of the stochastic kinematic anisotropies, basing on [20, 23]). In accordance with the introduction, it is established that the SGWB account contributions originating both within our galaxy and beyond. The extra-galactic components of the SGWB experience a Doppler shift relative to the source frame owing to the motion of our galaxy in relation to the rest frame

of the SGWB. Specifically, the behavior of the extra-galactic contributions to the SGWB is characterized by a sky-modulation of its apparent (frequency-dependent) energy density, denoted as $\Omega_{GW}(f, \hat{\mathbf{k}})$ and where we have made the general frequency and direction dependencies explicit. To illustrate, we consider two distinct cosmological frames: the first frame, denoted as \mathcal{S}' , is co-moving with the source of the SGWB and is referred to as the source frame. The second frame, denoted as \mathcal{S} , is in a state of constant velocity \mathbf{v} relative to \mathcal{S}' and serves as an observer frame. We make the assumption that the fractional energy density of the SGWB in the source frame, denoted as $\Omega'_{GW}(f)$, is perfectly isotropic and solely dependent on frequency f . This assumption is valid under the consideration that anisotropies intrinsic to the source are relatively small ¹. Consequently, without loss of generality, we employ a straightforward Lorentz boost transformation to map the SGWB density spectrum in the rest frame \mathcal{S}' , denoted as $\Omega'_{GW}(f)$, to the spectrum in the moving frame, denoted as $\Omega_{GW}(f)$, where $\mathbf{v} = \beta \hat{\mathbf{v}}$ represents the boost velocity ². For the energy density spectrum in particular, the boost mapping \mathcal{S}' to \mathcal{S} yields

$$\Omega(f, \hat{\mathbf{k}}) = \left(\frac{f}{f'}\right)^4 \Omega(f'). \quad (1)$$

The latter equation is most general for any Lorentz-boost where $0 \leq \beta < 1$. Following our assumption of a spectrum being isotropic in the source frame, we can expand this result up to second order on β , using the relations between f, f' outlined in [32], i.e.

$$\frac{f}{f'} = \mathcal{D} = \frac{\sqrt{1 - \beta^2}}{1 - \beta \hat{\mathbf{k}} \cdot \hat{\mathbf{v}}} \quad (2)$$

such that

$$\Omega_{GW}(f, \hat{\mathbf{k}}) = \mathcal{D}^4 \Omega'_{GW}(\mathcal{D}^{-1} f) \quad (3)$$

$$\Omega_{GW}(f, \hat{\mathbf{k}}) = \Omega'_{GW}(f) \left(1 + M(f) + \hat{\mathbf{k}} \cdot \hat{\mathbf{v}} D(f) + \left[\left(\hat{\mathbf{k}} \cdot \hat{\mathbf{v}}^2 - \frac{1}{3} \right) Q(f) \right] \right). \quad (4)$$

Here, the functions $M(f), D(f), Q(f)$ correspond to the monopole, dipole, and quadrupole contributions respectively. These functions are given by

$$M(f) = \frac{\beta^2}{6} (8 + n_\Omega(n_\Omega - 6) + \alpha_\Omega), \quad (5)$$

¹ Here, anisotropies arise from factors such as the initial production method of SGWBs, Sachs-Wolf (SW) and integrated SW effects, as well as from propagation through a perturbed universe.

² Throughout, we adopt the convention $c = 1$, such that $\beta = |\mathbf{v}| =: v$.

$$D(f) = \beta(4 - n_\Omega), \quad (6)$$

$$Q(f) = \beta^2 \left(10 - \frac{9n_\Omega}{2} + \frac{n_\Omega^2}{2} + \frac{\alpha_\Omega}{2} \right), \quad (7)$$

and

$$n_\Omega(f) = \frac{d \ln(\Omega'_{GW}(f))}{d \ln f}, \quad \alpha_\Omega(f) = \frac{dn_\Omega(f)}{d \ln f}. \quad (8)$$

It is crucial to acknowledge that the functions $M(f)$, $D(f)$, and $Q(f)$ introduced now are entirely model-dependent and encapsulate distinctive features corresponding to specific types of sources contributing to the extra-galactic segment of the SGWB. An expansion in $\hat{\mathbf{k}} \cdot \hat{\mathbf{v}}$ emerges as a consequence of the expansion in β . It is essential to highlight that $M(f)$, $D(f)$, and $Q(f)$ may acquire additional contributions beyond those specified in Equations (5)-(7) if intrinsic anisotropies are present in the spectrum of the source frame. As a result, Equation (4) when used in conjunction with $M(f)$, $D(f)$, and $Q(f)$ as defined, is only valid when anisotropies are absent from the source frame. As computationally evident, the aforementioned functions determine the harmonic expansion coefficients a_{lm} up to constant pre-factors. These coefficients play a fundamental role in shaping the angular power spectrum C_ℓ^{GW} . By rewriting (4) as

$$\Omega_{GW}(f, \hat{\mathbf{k}}) = \Omega'_{GW}(f) (1 + \delta_{GW}^{\text{kin}}(f, \theta, \phi)), \quad (9)$$

where δ_{GW}^{kin} now describes the anisotropic part of the measured energy density Ω_{GW} in the observer frame \mathcal{S} , we can exploit that δ_{GW}^{kin} has a smooth angular dependence, and expand as

$$\delta_{GW}^{\text{kin}}(f, \hat{\mathbf{k}}) = \sum_\ell \sum_m \delta_{GW, \ell m}^{\text{kin}}(f) Y_{\ell m}(\hat{\mathbf{k}}). \quad (10)$$

The angular power of the anisotropies is then given as an ensemble average

$$\langle \delta_{GW, \ell m}^{\text{kin}}, \delta_{GW, \ell' m'}^{\text{kin}} \rangle =: C_\ell^{GW}(f) \delta_{\ell \ell'} \delta_{m m'}. \quad (11)$$

The coefficient C_ℓ^{GW} can as well be derived by simply inserting the anisotropies $\delta_{GW}^{\text{kin}}(f, \hat{\mathbf{k}})$ in the latter equation. Then, by orthogonality of the spherical harmonics we find³

$$\begin{aligned} & \frac{1}{4\pi} \int_\Omega |\delta_{GW}^{\text{kin}}|^2 d\Omega \\ &= \sum_\ell \frac{1}{2\ell+1} \sum_m |\delta_{GW, \ell m}^{\text{kin}}|^2 =: \sum_\ell C_\ell^{GW}, \end{aligned} \quad (12)$$

³ Note that here we use the convention $\int_0^\pi d\theta \int_{\varphi=0}^{2\pi} Y_{\ell m} Y_{\ell' m'}^* d\Omega = \frac{4\pi}{(2\ell+1)} \delta_{\ell \ell'} \delta_{m m'}$.

therefore,

$$C_\ell^{GW} = \frac{1}{2\ell+1} \sum_{m=-\ell}^{\ell} |\delta_{GW, \ell m}^{\text{kin}}(f)|^2. \quad (13)$$

If we now combine this result with Equation (4), we can assign each mode for $\delta_{GW, \ell m}^{\text{kin}}$ to the corresponding kinematic mode, that is⁴

$$\begin{aligned} \delta_{GW, 00}^{\text{kin}}(f) &= 2\sqrt{\pi} M(f), & \delta_{GW, 10}^{\text{kin}}(f) &= 2\sqrt{\frac{\pi}{3}} D(f), \\ \delta_{GW, 20}^{\text{kin}}(f) &= \frac{4}{3} \sqrt{\frac{\pi}{5}} Q(f). \end{aligned} \quad (14)$$

It follows trivially that

$$\begin{aligned} C_0^{GW} &\sim |M(f)|^2, & C_1^{GW} &\sim |D(f)|^2, \\ C_2^{GW} &\sim |Q(f)|^2. \end{aligned} \quad (15)$$

It is crucial to underscore that the outlined decomposition offers distinct advantages. For instance, Equations (5)-(7) are determined by the gradient of the spectrum and its derivatives. It is easy to show that, in cases of a rapid change in the frequency spectrum, such as peaks or discontinuities, the individual components $M(f)$, $D(f)$, and $Q(f)$ experience an amplification in their amplitude, driven by the n_Ω and α_Ω . In some cases, we find that this amplification effect leads to the kinematic quadrupole dominating the kinematic dipole in the signal. The direct implications of such phenomena are discussed in section VI.

Choosing a particular instance for the spectrum Ω_{GW} , we leverage three principal examples of early universe cosmology that manifest in the SGWB. The significance of these signals arises from their anticipated amplitude and frequency range, aligning with the sensitivity of LISA [33], as illustrated in Figure 1. The main spectrum under consideration exhibits an approximate scale-free nature. In our analysis, it resembles the energy density spectrum of Cosmic Strings (CS), which is anticipated to manifest as a nearly slope-free spectrum [34–36] within the pertinent frequency range of LISA.⁵ Despite its simplicity, the analysis of CS features in the SGWB is intriguing, as CS serve as potent probes of physics beyond the Standard Model in the early universe and hold relevance in the context of string theory [37, 38]. The second spectrum under consideration is sourced by a first-order phase transition (PT) in the early universe

⁴ We here choose the frame where $\hat{\mathbf{k}} \cdot \hat{\mathbf{v}} \approx \cos \theta$. In subsequent sections, we transition to the International Celestial Reference System (ICRS) frame and concentrate on (3), albeit expressing it in terms of monopole, dipole, and quadrupole language utilizing the expansion coefficients $M(f)$, $D(f)$, and $Q(f)$.

⁵ For a given model i , the relevant frequency regime is defined as the intersection between the energy density Ω_{GW}^i and the region above the LISA sensitivity curve, as depicted in Figure 1.

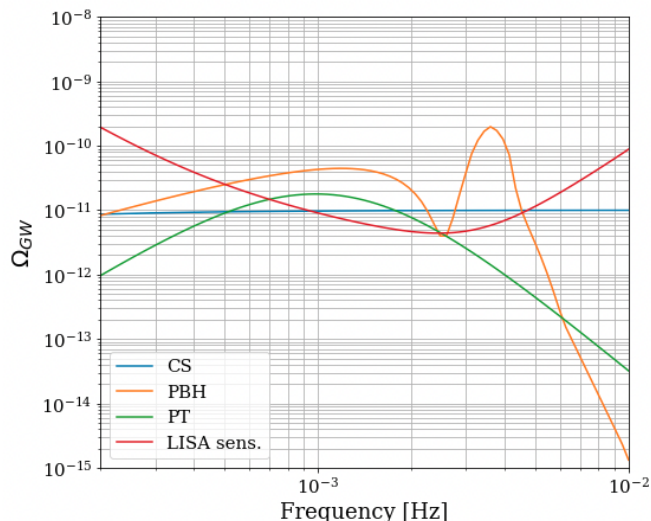


Figure 1. LISA sensitivity curve [33] compared to the expected stochastic GW spectrum for cosmic strings (blue) modeled as a scale-free contribution at a reference power of $\Omega_{GW} = 10^{-11}$, primordial black holes (green) modeled according to [41, 42], and first order phase transitions (red) as implemented in the PTPlot package [40]. For the LISA sensitivity curve we use the implementation within the PTPlot package.

and anticipated to follow a broken-power-law [39, 40] as depicted in Figure 1⁶. Phase transitions offer valuable phenomenological insights, notably marking scales of symmetry breaking occurring in the early universe.

Finally, our interest extends to the spectrum resulting from primordial black holes (PBH), as described in [41, 42]. However, it is acknowledged at this point that the literature lacks consensus on the exact shape in frequency space of PBH contributions to the SGWB. Regardless of the exact shape of the spectrum, the phenomenology associated with PBHs is extensive. Notably, models proposing Dark Matter compositions involving PBHs, either partially or entirely, have recently garnered significant interest within the scientific community [43, 44].

In the main analysis, i.e. section V, we focus on the simplest featureless model, the CS-like signal, and investigate its kinematic anisotropies through a realistic full-time domain simulation. The impact of more feature-full spectra such as the ones resulting from PT and PBH on the here presented analysis pipeline is discussed VI.

III. ANISOTROPIC GW STOCHASTIC SKY SIMULATION AND INSTRUMENT RESPONSE

This paper puts forth an end-to-end, time-domain simulation approach to generate realistic LISA data, coupled with a specialized analysis pipeline crafted for the identification of $l = 0, 1, 2$ (kinematic) anisotropies within a SGWB signal. To establish context, we describe the interplay between the detector's response and the SGWB signal in the following.

The SGWB signal can be modeled as a random, sky-dependent strain time-series $h_P(t, \hat{\mathbf{k}})$ of polarization P , following Gaussian statistics [24]. This time-series is fully characterized by the second-order moments of the Fourier transforms of the strain, denoted as $\langle h_P(f, \hat{\mathbf{k}}) h_{P'}^*(f, \hat{\mathbf{k}}) \rangle$. This expression defines the cross-power spectra $S_{PP'}(f, \hat{\mathbf{k}})$ of the stochastic process $h_P(t, \hat{\mathbf{k}})$. Under the assumption of statistical homogeneity, $\langle h_P(f, \hat{\mathbf{k}}) h_{P'}^*(f, \hat{\mathbf{k}}) \rangle$ corresponds to

$$S_{PP'}(f, \hat{\mathbf{k}}) = \begin{bmatrix} \langle h_+(f, \hat{\mathbf{k}}) h_+^*(f, \hat{\mathbf{k}}) \rangle & \langle h_+(f, \hat{\mathbf{k}}) h_\times^*(f, \hat{\mathbf{k}}) \rangle \\ \langle h_\times(f, \hat{\mathbf{k}}) h_+^*(f, \hat{\mathbf{k}}) \rangle & \langle h_\times(f, \hat{\mathbf{k}}) h_\times^*(f, \hat{\mathbf{k}}) \rangle \end{bmatrix} \\ = \frac{1}{2} \delta^2(\hat{\mathbf{k}} - \hat{\mathbf{k}}') \delta(f, f') \begin{bmatrix} I + Q & U + iV \\ U - iV & I - Q \end{bmatrix},$$

where one can introduce the Stokes parameters I, Q, U and V , well-known in CMB physics and encoding intensity, linear polarization and circular polarization respectively. As in [24], this analysis is restricted to the intensity $I(f, \hat{\mathbf{k}})$ with

$$I(f, \hat{\mathbf{k}}) = \langle h_+(f, \hat{\mathbf{k}}) h_+^*(f, \hat{\mathbf{k}}) \rangle + \langle h_\times(f, \hat{\mathbf{k}}) h_\times^*(f, \hat{\mathbf{k}}) \rangle \quad (16)$$

which can be related to the normalized logarithmic energy density $\Omega_{GW}(f, \hat{\mathbf{k}})$ as [45]

$$\Omega_{GW}(f, \hat{\mathbf{k}}) = \frac{32\pi^3 f^3}{3H_0^2} I(f, \hat{\mathbf{k}}), \quad (17)$$

where H_0 is the Hubble constant. Note here that the direction dependence of the latter two equations is commonly dropped by the assumption that

$$\Omega_{GW}(f, \hat{\mathbf{k}}) = \Omega_{GW}(f) \mathcal{E}(\hat{\mathbf{k}}). \quad (18)$$

The first factor on the right-hand side of Equation (17) remains applicable, while the second factor encapsulates the angular distribution of the background. We chose a normalization such that

$$\int_{S^2} d^2\hat{\mathbf{k}} \mathcal{E}(\hat{\mathbf{k}}) = 1. \quad (19)$$

With the stochastic strain h_P and the associated intensity $I(f, \hat{\mathbf{k}})$ at hand, we can now characterize the incoming signal as a time-frequency series. Following Equation (12) in [24], we define the signal component of the

⁶ Note that the exact shapes of the spectra, i.e. peak frequency f_{peak} or slope does not play a significant role in this analysis. Solely the fact that non-trivial n_Ω and α_Ω are achieved matters here.

time stream s_C^τ measured by a single TDI channel C as a Fourier expansion between t and $t + \Delta t$, such that it reads

$$s_C^\tau(f) = \sum_P \int_{S^2} d\hat{\mathbf{k}} R_C^{\tau,P}(f, \hat{\mathbf{k}}) h_P(f, \hat{\mathbf{k}}). \quad (20)$$

The superscript τ indicates that $s_C^\tau(f)$ is a potentially time-varying frequency series. In this expression, R_C^P represents the LISA response function, which depends on the selected channel $C \in [X, Y, Z]$ and the polarization $P \in [+, \times]$ of the strain. The elements R_C^P and the concept of channels will be discussed in the next subsection. Based on the definitions above, it holds that

$$\begin{aligned} & \langle h_P(f, \hat{\mathbf{k}}), h_{P'}^*(f', \hat{\mathbf{k}}') \rangle \\ &= \frac{1}{2} \frac{1}{4\pi} \delta_{f,f'} \delta^2(\hat{\mathbf{k}}, \hat{\mathbf{k}}') \delta_{P,P'} S_{PP'}(f, \hat{\mathbf{k}}). \end{aligned} \quad (21)$$

Under the Gaussian assumption, the power spectrum $S_P(f, \hat{\mathbf{k}})$ becomes the primary measurable quantity. The factor of 4π in the denominator arises from an integral over the unit sphere. While intensity is a quantity defined per pixel, the power spectrum density is an integral over the entire sky; hence, they differ by a factor of 4π . We can further assume that the SGWB is not polarized, so that $S_+(f, \hat{\mathbf{k}}) = S_\times(f, \hat{\mathbf{k}}) = \frac{1}{2} S_{GW}(f, \hat{\mathbf{k}})$ where the latter can be conveniently characterized by $\Omega_{GW}(f, \hat{\mathbf{k}})$ via [4]

$$S_{GW}(f, \hat{\mathbf{k}}) = \frac{3H_0^2}{4\pi^2 f^3} \Omega_{GW}(f, \hat{\mathbf{k}}). \quad (22)$$

$$y_{ij,p}(t) \approx \frac{1}{2(1 - \hat{\mathbf{k}}_p \cdot \hat{\mathbf{n}}_{ij}(t))} \left[H_{ij,p} \left(t - \frac{L_{ij}(t)}{c} - \frac{\hat{\mathbf{k}}_p \cdot \mathbf{n}_j(t)}{c} \right) - H_{ij,p} \left(t - \frac{\hat{\mathbf{k}}_p \cdot \mathbf{n}_i(t)}{c} \right) \right]. \quad (24)$$

In the latter, $L_{ij}(t)$ is the time-dependent separation between two spacecrafts defined via their positions $\mathbf{x}_i = \mathbf{x}_j + L_{ij} \hat{\mathbf{n}}_{ij}$ and $\hat{\mathbf{n}}_{ij}$ is the unit link vector. In the case of $c = 1$, $L_{ij}(t)$ corresponds to the delay time along the link ij at reception time t . The vector $\hat{\mathbf{k}}_p$ represents the wave vector of the GWs originating from pixel p , but also understood as the direction in the sky of the pixel p (in the plane wave approximation). The projection function $H_{ij,p}$ is given by

$$\begin{aligned} H_{ij,p}(t) &= h_+(t, \hat{\mathbf{k}}_p) \xi_+(\hat{\mathbf{u}}_p, \hat{\mathbf{v}}_p, \hat{\mathbf{n}}_{ij}) \\ &+ h_\times(t, \hat{\mathbf{k}}_p) \xi_\times(\hat{\mathbf{u}}_p, \hat{\mathbf{v}}_p, \hat{\mathbf{n}}_{ij}), \end{aligned} \quad (25)$$

where the functions ξ_+ and ξ_\times are the *antenna pattern functions* and $\hat{\mathbf{u}}_p, \hat{\mathbf{v}}_p$ the polarization vectors associated to the propagation vector $\hat{\mathbf{k}}_p$. For details, see appendix A in [2] and references therein.

To compute TDI observables, LISA combines the six link-signals resulting in three correlated channels commonly

Note at this point the similarities between Equations (17) and (22).

A. LISA response function

The three spacecraft composing the LISA instrument contain six distinct links, illustrated in Figure 2, each of which is deformed in a time-dependent manner by incoming gravitational radiation. Due to the linearity of the response function, the overall response of link $ij \in \{12, 21, 13, 31, 23, 32\}$ is given by the sum of individual responses to a source allocated in pixel p ,

$$\tilde{y}^\tau(f) = y_{ij}^\tau(f) = \sum_p y_{ij,p}^\tau(f). \quad (23)$$

Here again, we denoted time dependence via the superscript τ . The expression of the total link response in terms of response per pixel is required for numerical modeling, and is anyhow motivated by the limited resolution of the instrument. For every time step Δt , $y_{ij,p}$ can be understood as the frequency shift induced on the laser beam along the link ij by the gravitational strain originating in the pixel p . To obtain an explicit expression for $y_{ij,p}$, we hence have to project the strain from point source p onto the unit vector pointing along the link ij . Under the approximation of immobile spacecrafts during the light propagation along a single link, one finds [2]

referred to as X, Y, Z , illustrated in Figure 2. The explicit linear combination of links leading to the designated channels can be encapsulated in one matrix, \mathbf{M}_{TDI} [2]. For instance, the second generation TDI X_2 channel as it is sketched in Figure 2 can be constructed using links $y_{12}, y_{21}, y_{13}, y_{31}$,

$$\begin{aligned} X_2 &= X_1 + \mathbf{D}_{1321} y_{12} + \mathbf{D}_{131212} y_{21} + \mathbf{D}_{1312121} y_{13} \\ &+ \mathbf{D}_{13121213} y_{31} - (\mathbf{D}_{12131} y_{13} + \mathbf{D}_{121313} y_{31} \\ &+ \mathbf{D}_{1213131} y_{12} + \mathbf{D}_{12131312} y_{21}), \end{aligned} \quad (26)$$

with

$$\begin{aligned} X_1 &= y_{13} + \mathbf{D}_{13} y_{31} + \mathbf{D}_{131} y_{12} + \mathbf{D}_{1312} y_{21} \\ &- (y_{12} + \mathbf{D}_{12} y_{21} + \mathbf{D}_{121} y_{13} + \mathbf{D}_{1213} y_{31}). \end{aligned} \quad (27)$$

The delay operator for a single link is defined as

$$\mathbf{D}_{ij} x(t) = x(t - L_{ij}(t)), \quad (28)$$

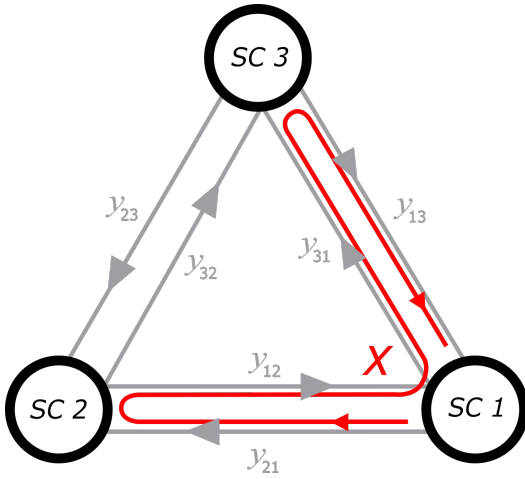


Figure 2. Illustration of three LISA spacecrafts in triangular formation, connected via six links (gray). Displayed in red is the 1.5 TDI X channel as a linear combination of links.

and can be accumulated forming the chained delay operator, $\mathbf{D}_{i_1, i_2, \dots}$, which, applied on a function $f(t)$, induces a chained delay in the reception, i.e.

$$\mathbf{D}_{i_1, i_2, \dots} f(t) = f\left(t - \sum_{l=1}^{n-1} L_{i_l, i_{l+1}}(t)\right). \quad (29)$$

Analogous construction can be done for the Y, Z channels by permuting ij in (27) and (26) correspondingly.

B. Analytical frequency domain response model and angular dependence

In the frequency domain, delay operators in the Equation 29 are expressed simply as phase operators. Using the analytical expression derived in Equation (B.5) of [2], we write in Equation 30 the single-link frequency series contributed from the unit sky-direction $\hat{\mathbf{k}}$ as the projection of the two polarizations to the frequency-domain response 2×6 (two polarizations, six links) kernel $G_{ij,P}^\tau(f, \hat{\mathbf{k}})$.

$$\tilde{\mathbf{y}}_p^\tau(f) = \sum_{P=(+, \times)} G_{ij,P}^\tau(f, \hat{\mathbf{k}}_p) h_p^\tau(f, \hat{\mathbf{k}}_p) \quad (30)$$

We will use the approximation that the transfer functions $G_{ij,P}^\tau(f, \hat{\mathbf{k}}_p)$ are stationary within the time segment labeled by τ , which implies time windows short enough relatively to the LISA orbital timescale ($\ll 1$ year). Then, one can structure the delay phase operators in a matrix form $\mathbf{M}_{TDI}^\tau(f)$ and whose time dependence (τ upper script) is induced by the annual orbital breathing of LISA constellation [2]. The measured data within a discrete time and frequency interval, $\tilde{\mathbf{d}}^\tau(f) \equiv (\tilde{X}, \tilde{Y}, \tilde{Z})^T$, can be expressed as a vector of TDI channels:

$$\tilde{\mathbf{d}}^\tau(f, \hat{\mathbf{k}}) = \mathbf{M}_{TDI}^\tau(f) \tilde{\mathbf{y}}^\tau(f, \hat{\mathbf{k}}), \quad (31)$$

with $\tilde{\mathbf{y}} = (\tilde{y}_{12}, \tilde{y}_{23}, \tilde{y}_{31}, \tilde{y}_{13}, \tilde{y}_{32}, \tilde{y}_{21})^T$ and where we made the time dependence an explicit argument of each tensor. Using definition (20) and the explicit formula for the individual link response, one can construct a three-vector (see appendix B in [2])

$$\mathbf{R}_P^\tau(f, \hat{\mathbf{k}}) = \mathbf{M}_{TDI}^\tau(f) G_{ij,P}^\tau(f, \hat{\mathbf{k}}) \mathbf{M}_{TDI}^\tau(f)^\dagger,$$

that contains the individual response components for each 1.5 TDI channel X, Y, Z . The subscript indicates the polarization dependence induced by the strain appearing in (20)⁷. The linear response TDI vectors $\mathbf{R}^P = (R_X, R_Y, R_Z)^P$ can be in turn merged into the quadratic response $\mathbf{A}^\tau (N_f \times N_\tau \times 3 \times 3 \times N_{\text{pix}})$:

$$\mathbf{A}^\tau(f, \hat{\mathbf{k}}) = \mathbf{R}^+ \otimes \mathbf{R}^{+*} + \mathbf{R}^\times \otimes \mathbf{R}^{\times*}, \quad (32)$$

such that the covariance matrix for a measured intensity \tilde{I} and noise matrix \mathbf{N} reads

$$\langle \mathbf{S}^\tau(f) \rangle = \mathbf{C}_f^\tau \approx \sum_p \mathbf{A}_p \tilde{I}^p + \mathbf{N}, \quad (33)$$

defined based on the quadratic strain tensor

$$\begin{aligned} \langle \mathbf{S}^\tau(f) \rangle &= \int_{S^2} d\hat{\mathbf{k}} \mathbf{s}^\tau(f) \otimes (\mathbf{s}^\tau(f))^* \\ &= \int_{S^2} d\hat{\mathbf{k}} \mathbf{A}^\tau(f, \hat{\mathbf{k}}) I(f, \hat{\mathbf{k}}). \end{aligned} \quad (34)$$

In the latter, we use a vector comprised of components (20) to construct a matrix in channel-space. In particular, Equation (34) and hence also the covariance matrix (33) itself are frequency- and direction-dependent time series of 3×3 matrices where the entries correspond to channels. Similarly, a TDI data vector recorded by LISA contains three components reflecting the three channels as mentioned above. Equation (31) can be decomposed into response, signal and noise via

$$\tilde{\mathbf{d}} = \mathbf{R}h + \mathbf{n}, \quad (35)$$

where the TDI noise \mathbf{n} is assumed to be Gaussian with zero mean and a covariance $\mathbf{N}_d = \mathbf{n} \otimes \mathbf{n}$. The data components are assumed to be Gaussian with covariance given by Equation (33). Note that $\tilde{\mathbf{d}}$ is again time and frequency dependent. However, note that the individual link response (23) is sensitive to the pixels in the sky and hence the direction. Consequently, so is \mathbf{R}^P . It is worth mentioning that there are analytical approaches for describing \mathbf{R}^P for the low frequency regime of LISA's sensitivity band, such as the one outlined in [24]. However, we aim to harness the power of numerical tools to provide a more realistic detection scenario and hence rely on the numerical implementations. More details are given in the subsequent subsection.

⁷ Compare also [24].

In Equation (34) the product $\mathbf{A}\tilde{I}$ is integrated over the full sky. However, with a realistic finite sky resolution one preferably rewrites the integral as the sum over pixels, i.e. $\mathbf{A}_p\tilde{I}^p$. Converting angular- to pixel-dependence results in the response matrix being a 3-dimensional $3 \times 3 \times N_{\text{pix}}$ frequency- and time-dependent matrix. Here, N_{pix} stands for the number of pixels. The covariance matrix, due to the full sky integration in (33), is direction-independent.

C. Spherical harmonics representation

For the purpose of this work, tracing over pixels is the preferred measure of full-sky summation, simply due to the numerical nature of these analyses. Nevertheless, on an analytical level, we can exploit the continuous basis of spherical harmonics to decompose the covariance matrix into individual modes. This results in analog decomposition of the intensity I and consequently the power spectrum Ω_{GW} similar to Equation (4). Note however that in contrast to (4) the decomposition in modes does not require any assumptions about the (kinematic) origin of the signal. Hence, this approach stays more agnostic with respect to the underlying model.

Although \mathbf{A} and I depend on the direction in the sky, in Equation (34) the Mollweide projection provides a bijective map transforming $\mathbf{A}(\hat{\mathbf{k}}) \rightarrow \mathbf{A}^p$ and vice versa. As a continuous map can be decomposed into spherical harmonics, the Mollweide map enables us at any point of our analysis to write the covariance matrix in terms of modes rather than pixels. In practice the mapping can be achieved as follows: Writing the sum over pixels explicitly, we can replace the latter by the approximation

$$\sum_p \mathbf{A}_p \tilde{I}^p \approx \frac{1}{\Delta_{\text{pixel}}} \int_{S^2} d\hat{\mathbf{k}} \mathbf{A}(\hat{\mathbf{k}}) \tilde{I}(\hat{\mathbf{k}}). \quad (36)$$

Here, Δ_{pixel} corresponds to the area per pixel⁸. Frequency and time dependence of both response matrix and intensity are omitted in the latter. Naturally, the approximation improves with the number of pixels. The latter equation can be simplified further by rewriting \mathbf{A} and I as

$$\mathbf{A}(\hat{\mathbf{k}}) = \sum_{\ell,m} a_{\ell,m} Y_{\ell,m}(\hat{\mathbf{k}}), \quad I(\hat{\mathbf{k}}) = \sum_{\ell,m} i_{\ell,m} Y_{\ell,m}(\hat{\mathbf{k}}) \quad (37)$$

where

$$\begin{aligned} \langle i_{\ell m}, i_{\ell' m'}^* \rangle &=: C_{\ell}^{GW} \delta_{\ell\ell'} \delta_{mm'}, \\ \langle a_{\ell m}, a_{\ell' m'}^* \rangle &=: \mathbf{A}_{\ell} \delta_{\ell\ell'} \delta_{mm'} \end{aligned} \quad (38)$$

⁸ Note that for most commonly used mappings of the Riemann sphere S^2 this area per pixel is not constant, however we will refer to suitable python packages taking care of this transformation.

and

$$C_{\ell}^{GW} = \frac{1}{2\ell+1} \sum_{m=-\ell}^{\ell} \left| \int_S \frac{d\hat{\mathbf{k}}}{4\pi} Y_{\ell,m}(\hat{\mathbf{k}}) I(\hat{\mathbf{k}}) \right|^2, \quad (39)$$

$$\mathbf{A}_{\ell} = \frac{1}{2\ell+1} \sum_{m=-\ell}^{\ell} \left| \int_S \frac{d\hat{\mathbf{k}}}{4\pi} Y_{\ell,m}(\hat{\mathbf{k}}) \mathbf{A}(\hat{\mathbf{k}}) \right|^2, \quad (40)$$

so that

$$\mathbf{A}_p I^p \rightarrow \int_{S^2} d\hat{\mathbf{k}} \sum_{\ell',m'} \sum_{\ell,m} a_{\ell m} i_{\ell' m'} Y_{\ell',m'}(\hat{\mathbf{k}}) Y_{\ell,m}(\hat{\mathbf{k}}). \quad (41)$$

Note though that, technically, we neglected the factor of the pixel area here and mathematical equality in the latter holds only in the limit of large pixel number. In either case, the right-hand side can be simplified by using that $Y_{\ell,-m} = (-1)^m Y_{\ell,m}^*(\hat{\mathbf{k}})$ and $i_{\ell,-m} = (-1)^m i_{\ell m}^*$ ⁹, and the orthogonality relation of the spherical harmonics. Then we find

$$\begin{aligned} & \int_{S^2} d\hat{\mathbf{k}} \sum_{\ell',m'} \sum_{\ell,m} a_{\ell m} i_{\ell' m'} Y_{\ell',m'}(\hat{\mathbf{k}}) Y_{\ell,m}(\hat{\mathbf{k}}) \\ &= \int_{S^2} d\hat{\mathbf{k}} \sum_{\ell,m} \sum_{\ell',m'} a_{\ell m} i_{\ell',-m'}^* Y_{\ell m}(\hat{\mathbf{k}}) Y_{\ell',-m'}^*(\hat{\mathbf{k}}) \end{aligned} \quad (42)$$

$$\begin{aligned} &= \int_{S^2} d\hat{\mathbf{k}} \sum_{\ell,m} \sum_{\ell',m'} a_{\ell m} i_{\ell',m'}^* Y_{\ell m}(\hat{\mathbf{k}}) Y_{\ell',m'}^*(\hat{\mathbf{k}}) \\ &= \sum_{\ell,m} a_{\ell m} i_{\ell m}^*, \end{aligned} \quad (43)$$

and thus

$$\mathbf{A}_p I^p \approx \frac{1}{\Delta_{\text{pixel}}} \sum_{\ell < 3} \sum_{m=-\ell}^{\ell} a_{\ell m} i_{\ell m}^*. \quad (44)$$

We sum only over $\ell = 0, 1, 2$, and the remaining modes are truncated, assuming that the signal intensity I is significant only up to $\ell = 2$, i.e., up to quadrupole contributions, analogous to (4). It is noted at this point that this is equivalent to setting $i_{\ell m} = 0$ for $\ell > 2$.

D. Data generation

Our proposal involves simulating the response of the LISA detector to a Doppler-boosted, anisotropic SGWB sky. Specifically, we aim to generate a synthetic dataset spanning 4 years, as outlined in Equation (35), with covariance given by Equation (33). For the data generation,

⁹ This relation only holds for the mode components of $I(\hat{\mathbf{n}})$ as the intensity is a real quantity, as opposed to the response.

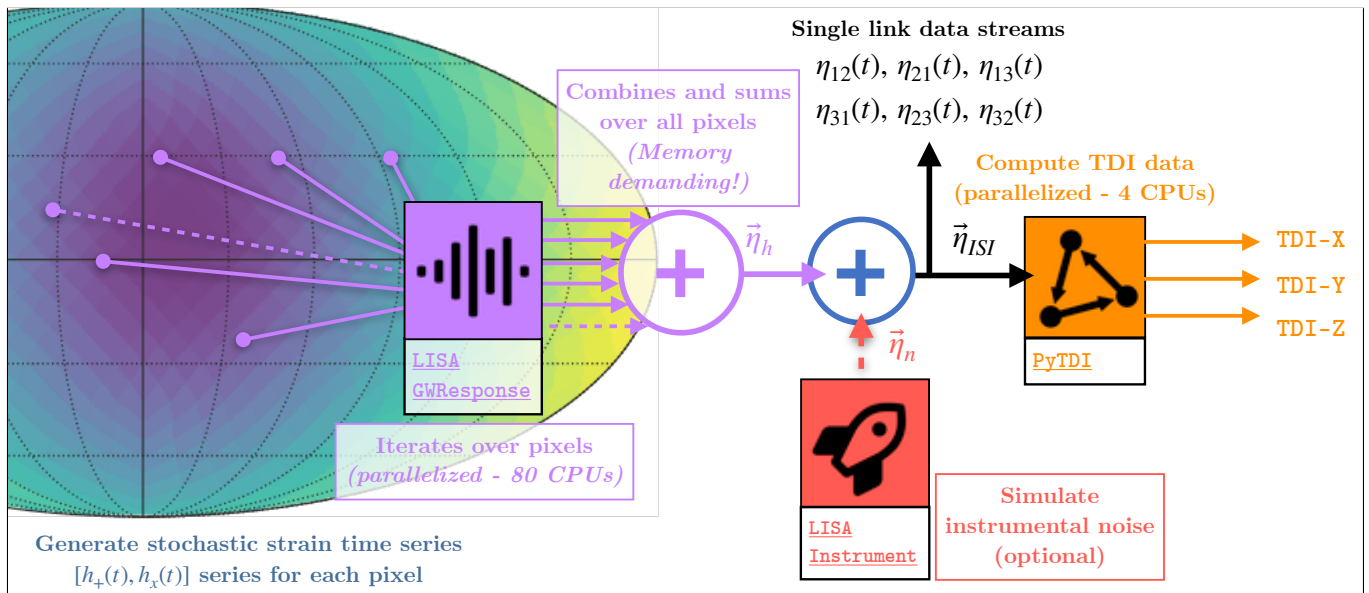


Figure 3. End-To-End (E2E) simulation flow of LISA response to an anisotropic, stochastic GW sky.

we will focus solely on the simple case of an SGWB with a flat energy density spectrum, such as potential CS signals in the LISA band [4].

For the generation of data, we employ an angular discretization of the sky into finite-size pixels using the python package `healpy`. The latter is extensively used throughout our analysis, providing a useful tool for mapping and the conversion from the pixel to mode domain. Each pixel of the generated $N_{\text{pix}} = 12 \times 2^{N_{\text{side}}}$ pixels sky map is simulated as an individual, independent stochastic strain time series of Power Spectral Density (PSD), S_h , as given in Equation (22). We emphasize here that, initially, we do not include instrumental noise or confusion foregrounds in the data. Hence, the first step of the analysis is solely dedicated to analyzing LISA's capabilities in dealing with faint signals of stochastic nature. Hereby, the complexity to be overcome resides in the randomness of the time series for each pixel in the sky (see Figure 3).

The LISA single-link responses to each individual pixel is computed using, as in [2], the `LISAGWResponse` software [25], part of the LISA consortium simulation suite, which provides a time-domain projection of h_+ and h_x polarization time series on the antenna response with minimal approximations¹⁰. In addition, a simplified orbital set-up is used, which considers an equilateral, equal arm configuration [26]. The linearity of the response function allows computing the overall response to an anisotropic GW sky as a net sum of the N_{pix} single pixel source responses. This projection is hence typically parallelized and distributed over up to > 80 CPUs, selecting an ad-

equated trade-off between CPUs and Memory usage (i.e. the more CPU-distributed, the more RAM demanding). For an $N_{\text{side}} = 32$ sky resolution, 4-years long dataset sampled at 0.2Hz, the data generation deployed on a computing node uses up to 128 CPUs and 3TB RAM over 15 hours or runtime. Particular attention should be set on the statistical independence across the stochastic pixel sources when parallel computation is performed. Each individual process initializes the random generators with a specific *local seed* while a *global seed* reshuffling the overall sky generation ensures statistical independence between simulation runs.

The single-link simulated data are subsequently processed using the LISA consortium `PyTDI` software [29] to generate the second-generation Time-Delay Interferometry (TDI) time-domain Michelson-like interferometer data streams $X_2(t)$, $Y_2(t)$, and $Z_2(t)$. Optionally, we introduce instrumental noise at the single-link level using the LISA simulation suite software `LISAInstrument`, enabling only the secondary noises for simplicity and efficiency, as the `PyTDI` software downstream is dedicated and designed to suppress the primary noises. Figure 3 summarizes the end-to-end simulation flow.

It is crucial to highlight that the clock frame with respect to which phase measurements are recorded and stamped has a critical impact, when beat note data streams are combined to produce the Time-Delay Interferometry (TDI) time-series. While using local spacecraft reference time to compose the X , Y , and Z data streams is physically correct, as they are all reducible to observations made on a single spacecraft located at the node of the Michelson-like interferometer [30], issues arise when combining these time-series (X , Y , and Z) based on different time frames. They need to be set to a common reference clock to be compared mathematically. We ob-

¹⁰ Such include a static spacecraft within arm light-travel timescale as well as first order GW propagation time expansion.

IV. DATA ANALYSIS AND MAP-MAKING

A. The map-making likelihood function

For our analysis, we employ 4 years of TDI 2.0 data streams sampled at 0.2 Hz. Initially, the data undergoes a pre-processing scheme involving frequency and time compression. The 4-year TDI data stream is partitioned into N_t time steps, effectively determining the angular resolution of the analysis. Further data compression is achieved by averaging over frequency windows of width n_j . Based on the X, Y, Z TDI channel data vector \mathbf{d} , one can determine the averaged data matrix as in [2]

$$\bar{\mathbf{D}}(\tau_i, f_j) \equiv \frac{1}{n_j} \sum_{k=j-\frac{n_j}{2}}^{j+\frac{n_j}{2}} \tilde{\mathbf{d}}(\tau_i, f_k) \otimes \tilde{\mathbf{d}}(\tau_i, f_k)^\dagger. \quad (45)$$

where the $N_t \times N_f \times 3$ data vectors $\tilde{\mathbf{d}}$ are the Fourier transforms of the time-split, simulated X, Y and Z time series. The matrix $\bar{\mathbf{D}}(\tau_i, f_j)$ is the tensor product across TDI channels of the data vectors $\tilde{\mathbf{d}}$, before averaging over the spectral window of width n_j for data compression. It measures the cross-spectral density of the TDI data streams. The statistical expectation of $\bar{\mathbf{D}}$ is the theoretical covariance $\mathbf{C}_d := \mathbf{C}_{[X,Y,Z]}$ of the TDI time series, which the Bayesian map-making method we use is ultimately solving for. The theoretical covariance \mathbf{C}_d matrix can be computed, for each time and frequency bin, as

$$\mathbf{C}_d(\tau_i, f_j) = \mathbf{A}_d(\tau_i, f_j, p) I(f, p) + \mathbf{N}_d(\tau_i, f_j), \quad (46)$$

where \mathbf{A} is the $N_t \times N_f \times 3 \times 3 \times N_{\text{pix}}$ matrix encoding the quadratic response function of the instrument [24], $I(f, p)$ is the GW intensity sky map N_{pix} -vector, both showing explicit frequency and angular (pixel) dependence. Note that, as before, the product $\mathbf{A}_d I$ is summed over pixels. \mathbf{N}_d is the $N_t \times N_f \times 3 \times 3$ covariance matrix of TDI noise, and is optionally enabled in the analysis. The intensity pixel map $I(p)$ contains the free parameter we aim to solve for in the analysis.

Aiming for a best-fit of the intensity map with respect to the input data, the appropriate probabilistic measure must be chosen based on the structure and statistical properties of the data vector $\tilde{\mathbf{d}}$. In this analysis, we employ a likelihood analysis based on the matrices $\bar{\mathbf{D}}(\tau_i, f_j)$ statistics. In Equation (45) we have seen that for each time segment τ , $\bar{\mathbf{D}}$ is a (3×3) random matrix built from the average of the outer product of n_j Gaussian distributed frequency series within the frequency window $[j - \frac{n_j}{2}, j + \frac{n_j}{2}]$. It implies that $\bar{\mathbf{D}} \propto \tilde{\mathbf{d}} \tilde{\mathbf{d}}^\dagger$ follows a Wishart distribution $\bar{\mathbf{D}} \sim W_{q=3}(n_j, \mathbf{C})$ [46], with \mathbf{C} is the covariance matrix of the Gaussian process $\tilde{\mathbf{d}}$. For $n_j \geq 3$ the probability density function¹¹ of $\bar{\mathbf{D}}$ reads [46]

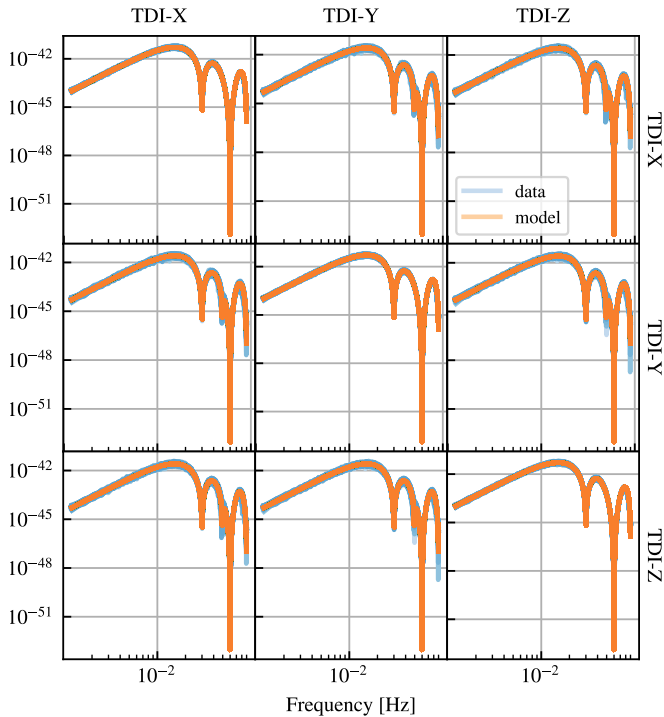


Figure 4. Averaged spectra of the 4-years-long data set compared to the space interferometer response model to an anisotropic GW sky. There are $N_t = 384$ spectra over plotted for each in the figure, in *shades of blue* for the data, and in *shades of red* for the model.

served that ignoring these relativistic corrections introduces significant biases in the sky map results, particularly on the dipole. Ensuring a common time frame for X, Y , and Z —specifically, the Barycentric Coordinate Time (TCB) associated with the Barycentric Celestial Reference System (BCRS) has alleviated this systematic bias and ultimately revealed the sought kinematic dipole, as will be detailed in the next section.

¹¹ The density function is valid with respect to Lebesgue measure on the cone of symmetric positive definite matrices.

$$f(\bar{\mathbf{D}}) = \frac{1}{2^{n_j q/2} \Gamma_q\left(\frac{n_j}{2}\right) |\mathbf{C}|^{n_j/2}} |\bar{\mathbf{D}}|^{(n_j - q - 1)/2} \exp\left\{-\frac{1}{2} \text{Tr}(\mathbf{C}^{-1} \bar{\mathbf{D}})\right\}. \quad (47)$$

Here, $\Gamma_q(\alpha)$ is the multivariate gamma function, and the dimension parameter $q = 3$ accounting for the three TDI channels. Based on the latter equation, we can now formulate the likelihood \mathcal{L} to maximize. Note that any constant prefactor will drop out in the logarithmic likelihood ratio computed by the MCMC sampling; hence, only the fitting parameters dependent factors are relevant.

For the purposes of this investigation, we define the log-likelihood function corresponding to a data sample $\bar{\mathbf{D}}$ as in Equation (45), i.e.

$$\log \mathcal{L} = \sum_{\tau_i} \sum_{f_j} \left[-\text{tr}(\mathbf{C}_d^{-1} \bar{\mathbf{D}}(\tau_i, f_j)) - \nu \log |\mathbf{C}_d(\tau_i, f_j)| \right], \quad (48)$$

where the trace is taken over the TDI channels. We have introduced the effective number of Degree of Freedom (DoF) $\nu = \frac{n_j}{N_{bw}}$, accounting for the reduction factor N_{bw} , also known as the normalized equivalent noise bandwidth [47], which depends on the time segments τ overlap and the window functions applied when time splitting the data¹².

It is evident that the fitting parameters enter via the covariance matrix \mathbf{C}_d and, within it, via the intensity map. The Bayesian map-making strategy necessitates the numerical computation of the covariant matrix \mathbf{C}_d for each step in the MCMC parameter space exploration, employing the left-hand side of Equation (36). While the evaluation of the log \mathcal{L} function requires the intensity pixel map I_p , several methods can be employed for extracting the relevant information from I_p using a minimal set of fitting parameters. For our investigations, we focus on the following two:

The first choice relies on the assumption that the anisotropies in the signal are produced by a Doppler boost. For a scale-invariant energy density spectrum, as given in Equation (4), a suitable reference frame can be fixed without loss of generality, leaving four parameters that determine the pixel map I_p , i.e. the monopole power in the observer frame, $\Omega'_{GW}(f)$, and three velocity components $\vec{\beta} = [\beta_x, \beta_y, \beta_z]$, as appearing in (4). These components are related to the boost vector of the solar system relative to the CMB frame and are expressed in the BCRS-frame. Combining Equations (3) and (17) yields the intensity I_p and, correspondingly, \mathbf{C}_d . The advantage of this model lies in its small number of fit parameters, significantly reducing the numerical complexity

of our pipeline. However, this technique is fully model-dependent, meaning it is only valid for Doppler-sourced anisotropies originating from a scale-free source being the dominant contribution in the cosmological SGWB.

Another approach of extracting the intensity map from a given model is through its decomposition into modes of the spherical harmonics' basis. In this scenario, the pixel map I_p is decomposed into 6 independent modes (considering only up to quadrupolar anisotropies, i.e. to $\ell = 2$), where the $\ell, \pm m$ modes are interdependent since I_p is real for every pixel. The 6 modes correspond to 9 independent parameters, as 3 of the relevant modes are complex. This decomposition is model-independent and, in principle, captures any anisotropy within the data, including intrinsic anisotropies in the source frame.

Note that both parametrization discussed above are only valid for a scale free spectrum. For more complex spectra, i.e. spectra with non-trivial spectral dependency, knowledge of the corresponding fit parameters is required for each frequency bin individually.

B. MCMC sampling and map reconstruction

In our investigation of the two parameter spaces, we seek the optimal fit for the intensity map, denoted as I_p , using simulated LISA data through MCMC sampling of the likelihood function outlined in Equation (48). Despite the computational demands associated with exploring the parameter space via MCMC, this approach offers a notable advantage by circumventing the numerically challenging Fisher matrix inversion. The latter inversion, when employed, can introduce systematics and compromise the overall robustness of the analysis [23, 24]. Moreover, beyond the numerical challenges, the analytical derivation of the Fisher iteration typically involves a Gaussian approximation, assuming the likelihood function approximates a Gaussian distribution near its peak [48]. In contrast, our MCMC scheme is not relying on any analytical or numerical approximations of the log-likelihood function in the Equation 48. As our focus is confined to low modes in the study of kinematic anisotropy, an MCMC map-making strategy based on the methodology presented in [24] becomes particularly pertinent. Furthermore, the inherent low angular resolution of LISA, limiting the resolution of higher modes, renders an MCMC map-making approach a practical and effective solution for many scenarios encountered in LISA analyses.

Our mapping scheme is structured as follows: At each iteration of the algorithm, the likelihood of Equation (3)

¹² we refer the reader to the comprehensive review [47] for further details

is evaluated based on the current state's location in the parameter space. In principle, the covariance matrix can be calculated by inserting Equation (4) into (48); however, numerically we are not bound to the necessity of expanding in small velocities and can instead use the full expression, (3), to calculate the \mathbf{C}_d and the likelihood correspondingly. As introduced in section II, for a flat and isotropic energy density spectrum $\Omega_{GW}(f)$ in the CMB-frame, the Doppler shift due to the observer's velocity with respect to stochastic emission induces a sky modulation of its amplitude that does not depend on the frequency, i.e. $\alpha_\Omega = n_\Omega = 0$. This implies that changing the velocity vector $\vec{\beta}$ will have an overall effect on the sky map at all frequencies, and the treatment of frequency and angular dependence remains separate,

$$\begin{aligned} \mathbf{C}(\tau, f) &= \mathbf{A}(\tau, f, p) I(f, p) \\ &= \mathbf{A}(\tau, f, p) \frac{E(f)}{E(f_0)} I(f_0, p) \end{aligned} \quad (49)$$

where we have extracted the spectral dependency of the energy density in the CMB-frame via the function $E(f)$ as in [24], and we use the (arbitrary) reference frequency of $f_0 = 1$ mHz to define the intensity map $I(p) = I(f_0, p)$ we are fitting for. Thus, for each iteration i , the evaluation of Equation (3) boils down to computing the prefactor (2) for the new velocity vector $\vec{\beta}^i$ when applying the model-dependent fit ansatz. Given the fit parameters $\{\Omega_{GW}^i, \beta_x^i, \beta_y^i, \beta_z^i\}$ of iteration i selected by an arbitrary walker of the MCMC the algorithm proceeds by calculating

$$I^i(f_0, p) = \frac{3H_0^2}{32\pi^3 f_0^3} \mathcal{D}^4(p) \Omega_{GW}^i(f_0) \quad (50)$$

with

$$\mathcal{D}(p) = \frac{\sqrt{1 - |\vec{\beta}^i|^2}}{1 - |\vec{\beta}^i| \left[\hat{\mathbf{k}} \cdot \hat{\beta}^i \right]_p}. \quad (51)$$

The angular or pixel dependence of $I(f_0, p)$ is introduced implicitly through the Doppler-boosting of Ω_{GW}^i from the source into the observer frame via \mathcal{D} . Note that in the case of a slope-free spectrum, such as for CS, $\Omega_{GW}(f) = \Omega_{GW}$ is constant.

The resulting discrete $I^i(f_0, p)$ is then summed over pixels, as in Equation (49), yielding the covariance matrix \mathbf{C}^i for the i -th iteration. With the newly acquired covariance matrix, the likelihood function (48) is computed, and the results are compared to those of the other walkers within the corresponding iteration. By the definition of the scheme, the walkers statistically favor the vicinity around high-likelihood points in parameter space. Eventually, they converge toward a maximum of (48) for the given input data. In principle, the MCMC can be initialized in an arbitrary state. Including any previous knowledge about the anticipated signal will most likely

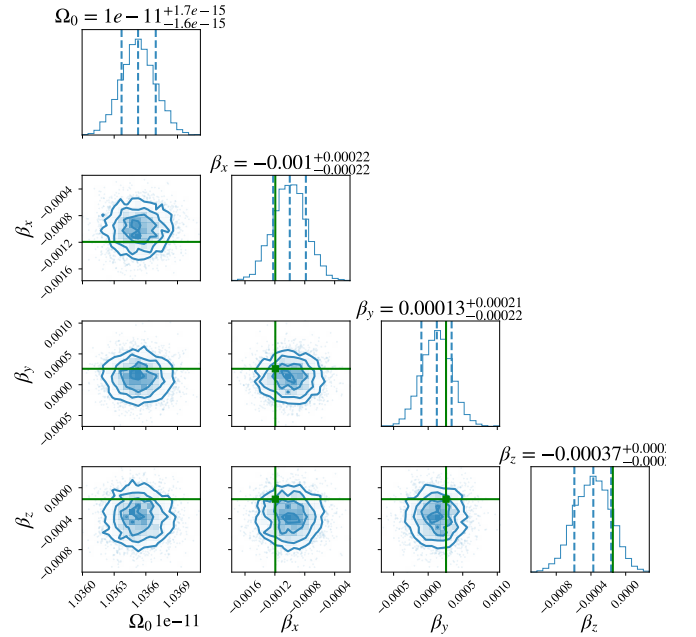


Figure 5. Samples histogram of the $(\Omega_{GW}, \vec{\beta})$ space for a single 4-years-long GW sky realization after convergence of the MCMC.

contribute to the scheme converging towards the correct maximum likelihood faster. Here, we favor an agnostic attempt, initializing the MCMC in an isotropic map configuration $\tilde{I}_p = \text{constant}$. For a detailed description of the specific MCMC scheme employed in this work, we refer to [49, 50].

In Figure 5, we display an exemplary histogram and correlation diagram of the MCMC chains after convergence, focusing on a single realization of the SGWB sky. The MCMC chains exhibit convergence towards the true velocity β^{true} . The statistical properties of the MCMC samples, capturing the posterior distribution, offer a theoretical estimate of the measurement precisions. For this specific sky realization, β^{true} is observed to be more than $4\text{-}\sigma$ away from zero, indicating the detection of the observer's motion with respect to the CMB rest frame. Figure 6 reconstructs the recovered skymap from the β^{meas} measurement in Figure 5. We verified an excellent match between the input and output intensity maps, considering that the prior, starting point sky map was perfectly isotropic.

While the results from Figures 5 and 6 suggest the feasibility of resolving kinematic anisotropies with the MCMC map-making strategy, it is essential to acknowledge that, at this stage, the analysis remains susceptible to potential statistical fluctuations in the input sky map realization, leading to a fortuitous enhancement of the dipolar signal far from its expectation value. We refer to this signal-induced statistical fluctuation of the $\ell = 1, 2$ kinematic modes as ‘‘cosmic variance’’, drawing an analogy to the term as defined in the context of the CMB, where the measured positions of the peaks in the spectrum are lim-

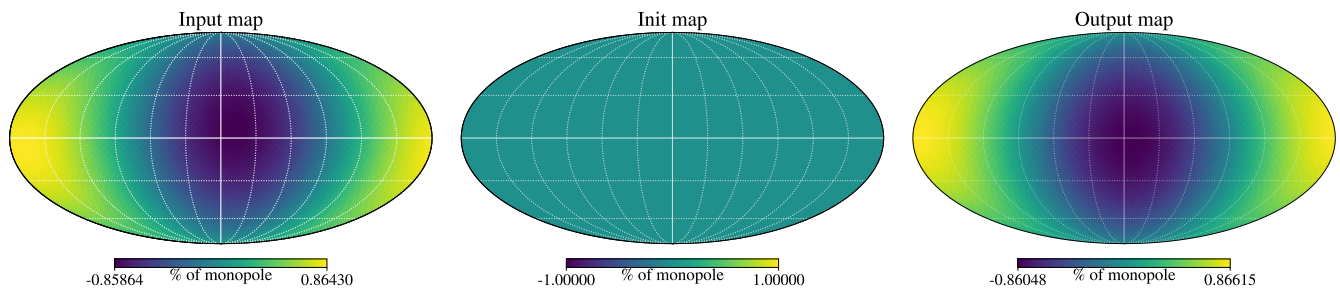


Figure 6. Intensity GW sky maps (in percentage of the monopole Ω_0). From left to right: the input intensity map injected, the a priori map used to initialize the MCMC chains, and the map recovered by the map-making algorithm. The monopole is removed from the intensity maps, to ease the visualization the dipolar anisotropy. These projection plots have been made from `healpy` python package.

ited by the fact that there is only a single realization of the spectrum observable from Earth [51]. Additionally, it is crucial to consider the possibility of an unfortunate systematic in the analysis that could have contributed to the observed signal.

V. ANALYSIS RESULTS

In the following section, we will delve further into investigating the analysis artifacts discussed above and demonstrate that they can be excluded as plausible sources contributing to the observed signals in Figures 5 and 6.

To test against cosmic variance, we generate 30 independent realizations of the GW sky and reiterate the map-making procedure outlined in Section IV B for each realization in V A. Subsequently, in section V B, the input sky map is rotated arbitrarily to verify the congruence between the injected and recovered intensity maps, excluding systematic errors as an explanation for the observed signal. To achieve this analysis, we introduce instrumental noise to the simulation to assess Signal-to-Noise Ratio (SNR) and discuss the detectability of scale-free SGWB kinematic anisotropies for LISA in section V D.

A. Statistical significance and cosmic variance

The statistical robustness of the signal depicted in Figures 5 and 6 is assessed through a comparison of 30 randomly generated realizations of a stochastic GW sky. Figure 7 illustrates the dispersion of the measured velocity β^{meas} in the SGWB rest frame with respect to each distinct realization of the SGWB. The figure also presents a comparison between the mean value and standard deviation over the 30 realizations, alongside the true velocity values and theoretical uncertainty estimates from the MCMC sampling. The analysis in Figure 7 shows that the statistics of the 30 measurements align well with the theoretical values. Specifically, the average $\bar{\beta}^{\text{meas}}$ converges towards β^{true} , and the measured standard devi-

ation is compatible with the theoretical error bars. Notably, the average measured $\bar{\beta}_x^{\text{meas}}$ is well resolved and located $> 4\sigma$ away from 0. This numerical demonstration establishes that even in the challenging and poor-featured scenario of a boosted, scale-free CS-like stochastic signal, the inherent *cosmic variance* is effectively overcome. Based on the 30 realizations, we also compute the asso-

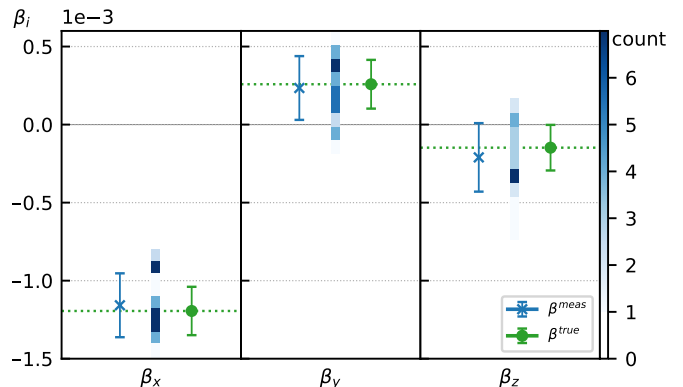


Figure 7. Variance of the measured signal over the 30 realizations of the GW sky (blue histograms), compared to the resulting averaged values and standard deviations (in blue), and the theoretical values and MCMC error bars (in green). Are plotted the data for β_x , β_y and β_z , from left to right. The dispersion of β^{meas} realizations are statistically consistent with the true values β^{true} and the theoretical error bars from the MCMC sampling. β_x is resolved $> 4\sigma$ away from 0.0 value.

ciated intensity maps and their $a_{\ell m}$ components in the spherical harmonics decomposition. In Figure 8, we conduct the same statistical studies to verify the robustness of the resolution of kinematic spherical harmonics mode and observe a clear measurement of the dipolar, unambiguous (1, 1) mode, which constitutes the principal component of the boosted SGWB data with a flat energy density spectrum. Here, the $\ell = 1$ modes are, as anticipated, orders of magnitude brighter than the $\ell = 2$ modes, given their intensity scales as β^ℓ . However, notably, the MCMC

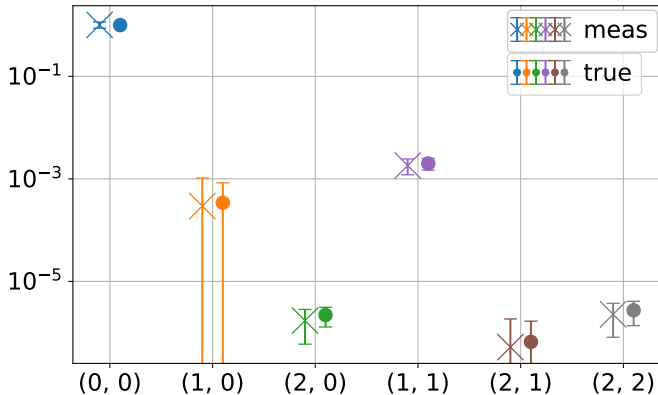


Figure 8. Variance of the measured signal against the theoretical error bars for the mode components of the SGWB in the observer frame up to $\ell = 2$ based on the statistics for β_i , Figure 7.

starts to exhibit sensitivity to quadrupolar components such as the (2,0) and (2,2) modes, detected here approximately with an 2σ confidence level. This sensitivity arises from the fact that LISA is significantly more responsive to quadrupolar signals than to dipolar signals due to the pronounced parity of its response [32] [23]. This enhanced response partially compensates for the intrinsic weakness of the quadrupolar component, bringing it within the observational reach of LISA. In some cases, cosmological signals with richer spectral signatures can further enhance the $\ell = 2$ component, and it is possible that $\ell = 2$ modes may become comparable or even the dominant kinematic signatures in the observed signal.

B. Systematic check

Having established the statistical significance of the result in Section IV B, we now address the possibility that the observed signal may be attributed to biases or systematic errors in the instrument response or the analysis. To scrutinize this aspect, we introduce a Doppler-induced anisotropic sky map by injecting a rotated velocity vector $\vec{\beta}^{\text{rot}}$. Subsequently, we verify our ability to recover this modified injection. The new velocity vector to be recovered is given by $\vec{\beta}^{\text{rot}} = R_{ZYX}(\phi, \eta, \theta) \vec{\beta}^{\text{true}}$, where the rotation matrix $R_{X,Y,Z}$ contains the angles $\phi = 100^\circ$, $\eta = 0^\circ$, $\theta = 60^\circ$ representing the Euler rotation angles around the Z, Y and X axes (of the SSB frame) respectively. Figure 9 displays the injected values $\vec{\beta}^{\text{rot}}$ and the recovered values for 10 realizations of the sky. Similar to Figure 7, the analysis successfully captures this newly injected signal. This observation demonstrates that the presented analysis pipeline can accurately reconstruct the injected sky map, providing evidence that the measured intensity map in Figure 6 is not attributable to a system-

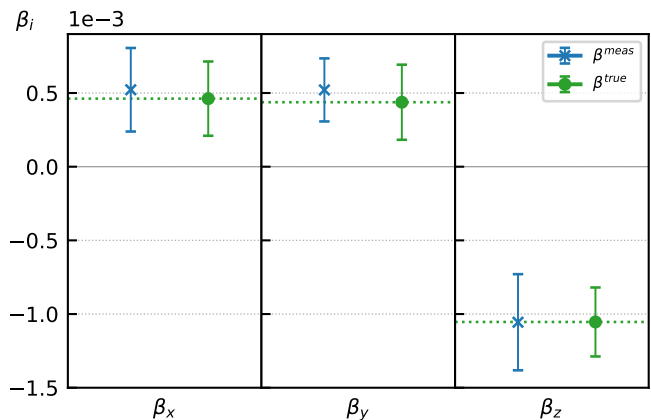


Figure 9. Variance of the measured signal over the 10 realizations of the *rotated* GW sky (blue histograms), compared to the resulting averaged values and standard deviations (in blue), and the theoretical values and MCMC error bars (in green). Are plotted the data for β_x^{rot} , β_y^{rot} and β_z^{rot} , from left to right. We do verify that new, modified input velocity β^{rot} is recovered with identical precision that in Figure 7

atic error.

C. Model-independent analysis

So far, the analysis focuses on the model-dependent ansatz for the choice of the fit parameters, i.e. we were fitting with respect to $\{\Omega_{GW}, \vec{\beta}\}$. We now switch to the fully agnostic approach and employ a fit for the spherical modes of the signal, parameterizing the intensity map I_p using its mode decomposition $i_{\ell m}$, see (37), up to $\ell \leq 2$. Note that under the assumption that the signal is of purely kinematic nature, i.e. results from the Doppler-boost of an isotropic background, the set $\{\Omega_{GW}, \vec{\beta}\}$ represents the minimal number of parameters to characterize the signal. In a general setting, however, a model-independent analysis enhances the versatility of the outlined pipeline. In contrast to the model-dependent ansatz, using the modes $i_{\ell m}$ enables the resolution of any angular dependence in the signal I_p , including both intrinsic or Doppler-induced sky anisotropies. As before, we analyze the model-independent choice of fit parameters for 10 random implementation of a CS-like SGWB signals. For each iteration k , the intensity I_p^k is computed via the modes $i_{\ell m}^k$ selected by the MCMC based on the likelihood function (48). The results are displayed in Figure 10. We observe that for $\ell = 0, 1$, the model-independent approach matches the accuracy of the parametrization $\{\Omega_{GW}, \vec{\beta}\}$. The measured mean values $\bar{i}_{\ell m}$ are statistically significant and exhibit a variance comparable to the theoretical error bars. Allowing for $\ell = 2$, the MCMC converges towards an undesirable maximum, largely overestimating the monopolar and quadrupolar contributions. This is partially due to

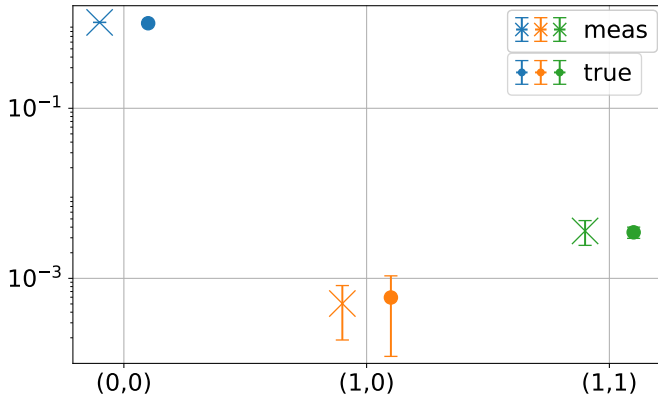


Figure 10. Variance of the measured signal against the theoretical error bars for the mode components of the SGWB in the observer frame up to $\ell = 1$ based on a MCMC-sampling using $a_{\ell m}$.

the correlation between monopole and quadrupole manifesting in an equal power in β carried by both, see Equation (5) and (7), and which is confirmed numerically. We are led to the conclusion that, due to the correlation of M and Q , the model-independent approach allows for statistical uncertainties of the monopole to leak into the quadrupole. The consequence of this leakage resides in mono- and quadrupole reaching similar orders of magnitude in the output skymap I_p^{out} . This undesirable effect can be counteracted by fine-tuning analysis parameter such as frequency- and time-binning, or disentangling mono- and quadrupole via different parametrizations. One could also think of recursive schemes by which we first fix $\ell = 0, 1$ via the MCMC before fitting for $\ell = 2$ only. All options have been considered, however no optimal strategy has been identified so far. We leave a deeper investigation to future works.

D. Instrumental noise and detectability prospects of boosted scale-free SGWB

At this stage, instrumental noise has not been incorporated. The inherent stochastic characteristics of the signal, specifically the intrinsic variance of its spectrum density competing with its annual temporal fluctuations, has constituted the exclusive sources of randomness and uncertainty under consideration. As illustrated in Figure 7, the precision of the map-making process surpasses the anticipated cosmic variance for a data span of 4 years. Importantly, this outcome has remained entirely unaffected by the signal amplitude Ω_{GW} in the noise-free case, which has not been a subject of discussion hitherto.

To investigate the detectability (i.e. including instrumental noise) of Doppler boost-induced anisotropies in a scale-free extra-galactic SGWB, we now take the instrumental noise into consideration. We adopt a zero-

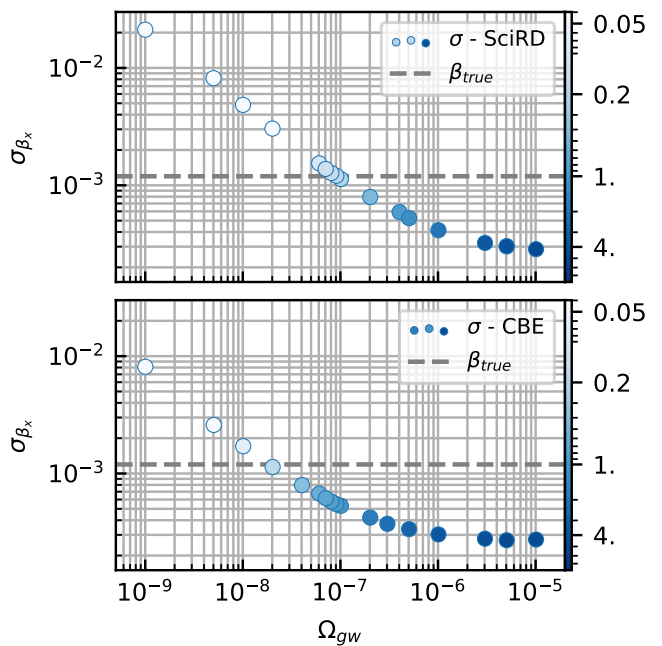


Figure 11. Analysis of the evolution of σ_{β_x} as the signal amplitude Ω_{GW} varies. The blue color bar provides the estimated standard deviation $\frac{\sigma_{\beta_x}}{|\beta_x^{\text{true}}|}$ in $|\beta_x^{\text{true}}|$ unit. Two instrumental noise models are considered: SciRD specifications (top) and current best estimate (down), differing essentially by the level of OMS noise (displacement noise floor at 1.5×10^{-11} and $6.35 \times 10^{-12} \text{ m Hz}^{-1/2}$ resp. [27, 33]). Both cases confirm that the kinematic dipole is reachable for Ω_{GW} values typically above 10^{-7} . We observe that for $\Omega_{GW} > 10^{-7}$ we converge to the cosmic variance limit displayed in Figure 7.

noise likelihood MCMC map-making approach. In this methodology, we calculate the covariance matrix (46) by considering an expected value for the noise matrix \mathbf{N}_d derived from the noise model detailed in [2]. While the data matrix \mathbf{D} in the log-likelihood definition (48) remains unaltered, the modeled covariance matrix \mathbf{C}_d now incorporates instrumental noise, influencing the uncertainties associated with β^{meas} assessed through the MCMC analysis. Figure 11 presents the results of this analysis. In contrast to the approach in [2], we consider two noise performance scenarios: one conservatively aligned with the LISA Science Requirement Document (SciRD) [33], and a second more optimistic scenario in accordance with our current best understanding of the instrument's performance (see Appendix B and Eq. (B5) in [27]). The figure illustrates the estimated $\sigma_{\beta_x}^{\text{mcmc}}$ as a function of Ω_{GW} , with the color scale indicating, for each data point, the distance to the target β_x^{true} in units of $\sigma_{\beta_x}^{\text{mcmc}}$. Figure 11 affirms the findings reported in [23]. In the top subplot, under a conservative noise configuration, we find that the observability of the kinematic dipole becomes significant only at relatively large values of $\Omega_{GW} \gtrsim 10^{-7}$. The more optimistic scenario, utilizing the latest LISA performance model, indicates detectabil-

ity at $\Omega_{GW} \gtrsim 5 \times 10^{-8}$, potentially reaching 10^{-8} . This order of magnitude aligns with expectations, considering LISA's suboptimal sensitivity to odd- ℓ modes [23].

With this comprehensive analytical tool at our disposal, we are poised to explore avenues for improving detectability. This involves optimizing the preprocessing of the TDI data streams through time-frequency analysis, considering more realistic orbital parameters, or leveraging spectral features in the SGWB to enhance both dipolar and quadrupolar kinematic anisotropies.

VI. SUMMARY AND DISCUSSION

In this article, a full time-domain map-making scheme based on a maximum-likelihood MCMC tailored to LISA and targeting kinematic anisotropies in the SGWB is presented. We generated stochastic strain time series for each pixel of the sky and projected it to the simulated, full instrument response function. For the resulting data streams consisting of channeled random data matrices convoluted with the instrumental response kernel, we selected a suitable model-based likelihood function to test the data against a physical model. Based on the selected likelihood function, a novel MCMC mapping scheme was developed. The efficacy of our pipeline was demonstrated by successfully recovering the injected map of Doppler-boosted primordial anisotropic data, showcasing the functionality of the MCMC-based mapping scheme for LISA. Our results indicate that our pipeline surpasses cosmic variance limitations in LISA data and exhibits robustness against systematical and statistical errors. The recovery of injected data was achieved using both model-dependent and independent sets of fit-parameters. Incorporating instrumental noise, we determined that the pipeline converges towards a statistically meaningful recovery of the kinematic dipole for $\Omega_{GW} \gtrsim 10^{-7}$ when conservative noise scenarios are applied, and slightly better for more favorable instrumental noise realizations¹³. These findings align with and complement the results reported in [23].

Despite these promising results of our analysis, we acknowledge areas for improvement that will be incorporated in the pipeline in future works. Specifically, we identified opportunities to optimize the data sampling process by switching to a time-frequency domain instead of a full, time-domain analysis. Replacing the short-Fourier transform with a wavelet-based analysis in the preprocessing phase can enhance the likelihood of recovering kinematic anisotropy from the data. Furthermore, we observed that the orbit dynamics have a significant impact on the output of the map-making scheme,

suggesting that simulating more realistic orbit dynamics, as opposed to the static equal-arm-length assumption applied here, helps to enrich the kinematic signatures in the data. We have observed, however, that the use of more realistic keplerian orbits introduce important biases in the map-making analysis, which are still under investigation. They seem to be tightly related to the initial preprocessing step, where the 4 years TDI data streams are time split using 50% overlapping Hanning windows. We believe that moving to a time-frequency representation of the TDI data will help fixing this issue, in the aim of exploiting the complex temporal features the full orbital dynamics provides to the response. More generally, we wish to address the sensitivity of the proposed map-making scheme to relevant parameters of the analysis, in particular the number of time- and frequency bins, n_{samples} and n_{avg} , in which the input data is divided¹⁴. We found that the convergence of the MCMC reacts sensitively to the choice of n_{samples} and n_{avg} . In particular, the monopole can be offset significantly for suboptimal choices of bin size. For the results displayed in the previous section, the parameters n_{samples} and n_{avg} were optimized with respect to the random walkers' convergence in the parameter space. While the implications of a shifted time (or frequency) grid within the context of the MCMC are not yet fully understood, they are currently being investigated and will be subject to future works. Again, we expect that the use of wavelet transforms will facilitate these investigations.

Finally, it is imperative to address more intricate primordial contributions to the SGWB exhibiting a non-trivial spectral dependency, see e.g. Figure 1. In the analysis above, we only considered a scale free spectrum motivated by CS contributions. However, extending this analysis to richer signatures can significantly improve the lower bound on Ω_{GW} for which the MCMC recovers the desired contribution. This statement is attributed to the dependence of the components $D(f)$ and $Q(f)$ on the slope, as outlined in Equations (6) and (7). Both functions, effectively representing dipole and quadrupole modes of the signal, exhibit notable amplifications when the slope of the spectrum Ω_{GW} varies with frequency. This variation is quantified by the functions n_{Ω} and α_{Ω} . In certain instances, this can result to the quadrupole power surpassing that of the dipole. Consequently, spectra originating from phenomena such as, for instance, PTs or PBHs strongly amplify the power of the kinematic anisotropies for $\ell > 0$, with a notable emphasis on enhancing the quadrupole. The augmentation of signal power for $\ell = 2$ is particularly significant for LISA, as the instrument exhibits heightened sensitivity to the quadrupolar mode of sky anisotropies [23].

Aside from the identification of cosmic origins of

¹³ Here, Ω_{GW} refers to the monopole power of the isotropic signal in the source frame.

¹⁴ Compare with Equation (45) and subsequent passages.

signatures in LISA data, our pipeline can be exploited to analyses galactic contributions to the SGWB as well. In this work, we build a framework assuming that an effective foreground removal scheme has been applied to the raw data. This step is highly non-trivial but falls out of the scope of this article. However, our map-making algorithm can very well be exploited for the mapping of the galactic confusion noise. The capability of the developed MCMC-mapping scheme to map the remaining Milky Way GW sources in LISA Data Challenge (LDC) data after extracting resolved binaries will be addressed in a follow-up project. In conclusion, this analysis presents a ready-to-use toolkit enabling tests of suitably processed LISA data of SGWB-nature for signatures of cosmic origin. Concretely, given the LISA sensitivity band being swamped by a SGWB signal, signatures rich in spectral features may be recovered for $\Omega_{GW} \gtrsim 10^{-8}$ given a less conservative instrumental noise realization. This utility becomes crucially relevant in the case of possible PTA signatures of a stochastic background [6] extending into the LISA band. If the latter signal is (partially) of cosmic origin, one expects very relevant contributions of the same source in LISA data band. A cosmic character of these hypothetical signatures can be established using the

here presented analysis pipeline.

ACKNOWLEDGEMENTS

LH would like to acknowledge financial support from the European Research Council (ERC) under the European Unions Horizon 2020 research and innovation programme grant agreement No 801781. LH further acknowledges support from the Deutsche Forschungsgemeinschaft (DFG, German Research Foundation) under Germany's Excellence Strategy EXC 2181/1 - 390900948 (the Heidelberg STRUCTURES Excellence Cluster). The authors thank the Heidelberg STRUCTURES Excellence Cluster for financial support. The authors acknowledge support by the state of Baden-Württemberg, Germany, through bwHPC. Computations were also performed on the DANTE platform, APC, France. The authors would like to thank Q. Baghi, J-B. Bayle, M. Besançon and N. Karnesis for their precious insight and the numerous fruitful discussions we had along this project. The authors also thank the LISA Simulation Working Group and the LISA Simulation Expert Group for the lively discussions on all simulation-related activities.

-
- [1] LIGO Scientific Collaboration and Virgo Collaboration, B. P. Abbott, R. Abbott, et al. Binary Black Hole Mergers in the First Advanced LIGO Observing Run. *Physical Review X*, 6(4):041015, October 2016.
- [2] Quentin Baghi, Nikolaos Karnesis, Jean-Baptiste Bayle, Marc Besançon, and Henri Inchauspé. Uncovering gravitational-wave backgrounds from noises of unknown shape with LISA. *Journal of Cosmology and Astroparticle Physics*, 2023(04):066, April 2023. Publisher: IOP Publishing.
- [3] Olaf Hartwig and Martina Muratore. Characterization of time delay interferometry combinations for the LISA instrument noise. *Physical Review D*, 105(6):062006, March 2022. Publisher: American Physical Society.
- [4] Chiara Caprini and Daniel G. Figueroa. Cosmological Backgrounds of Gravitational Waves. *Classical and Quantum Gravity*, 35(16):163001, August 2018. arXiv:1801.04268.
- [5] Michele Maiorano, Francesco De Paolis, and Achille A. Nucita. Principles of gravitational-wave detection with pulsar timing arrays. *Symmetry*, 13(12):2418, dec 2021.
- [6] Gabriella Agazie, Akash Anumalapudi, Anne M. Archibald, et al. The NANOGrav 15-year Data Set: Evidence for a Gravitational-Wave Background, June 2023. arXiv:2306.16213 [astro-ph, physics:gr-qc].
- [7] Adeela Afzal, Gabriella Agazie, Akash Anumalapudi, et al. The NANOGrav 15-year Data Set: Search for Signals from New Physics, June 2023. arXiv:2306.16219 [astro-ph, physics:gr-qc, physics:hep-ph].
- [8] Pau Amaro-Seoane, Heather Audley, Stanislav Babak, et al. Laser Interferometer Space Antenna. *arXiv:1702.00786 [astro-ph]*, February 2017. arXiv:1702.00786.
- [9] B. P. Abbott, R. Abbott, Acernese, et al. An upper limit on the stochastic gravitational-wave background of cosmological origin. *Nature*, 460(7258):990–994, August 2009. Number: 7258 Publisher: Nature Publishing Group.
- [10] The LIGO Scientific Collaboration, the Virgo Collaboration, the KAGRA Collaboration, and R. Abbott et al. The population of merging compact binaries inferred using gravitational waves through gwtc-3, 2022.
- [11] Arianna I. Renzini, Boris Goncharov, Alexander C. Jenkins, and Pat M. Meyers. Stochastic gravitational-wave backgrounds: Current detection efforts and future prospects, 2022.
- [12] Marica Branchesi, Michele Maggiore, David Alonso, et al. Science with the einstein telescope: a comparison of different designs. *Journal of Cosmology and Astroparticle Physics*, 2023(07):068, jul 2023.
- [13] Michele Maggiore, Chris Van Den Broeck, Nicola Bartolo, et al. Science case for the einstein telescope. *Journal of Cosmology and Astroparticle Physics*, 2020(03):050–050, mar 2020.
- [14] Matthew Evans, Alessandra Corsi, Chaitanya Afle, et al. Cosmic explorer: A submission to the nsf mpac ngw subcommittee, 2023.
- [15] David Reitze, Rana X Adhikari, Stefan Ballmer, et al. Cosmic explorer: The u.s. contribution to gravitational-wave astronomy beyond ligo, 2019.
- [16] Giorgio Mentasti, Carlo R. Contaldi, and Marco Peloso. Probing the galactic and extragalactic gravitational wave backgrounds with space-based interferometers, December 2023. arXiv:2312.10792 [astro-ph, physics:gr-qc].

- [17] Daniele Bertacca, Angelo Ricciardone, Nicola Bellomo, et al. Projection effects on the observed angular spectrum of the astrophysical stochastic gravitational wave background. *Physical Review D*, 101(10):103513, May 2020. arXiv:1909.11627 [astro-ph, physics:gr-qc].
- [18] N. Aghanim, C. Armitage-Caplan, M. Arnaud, et al. Planck 2013 results. XXVII. Doppler boosting of the CMB: Eppur si muove. *Astronomy & Astrophysics*, 571:A27, November 2014. Publisher: EDP Sciences.
- [19] Camille Bonvin, Ruth Durrer, and Martin Kunz. Dipole of the luminosity distance: A direct measure of $h(z)$. *Physical Review Letters*, 96(19), may 2006.
- [20] Giulia Cusin and Gianmassimo Tasinato. Doppler boosting the stochastic gravitational wave background. *Journal of Cosmology and Astroparticle Physics*, 2022(08):036, August 2022. Publisher: IOP Publishing.
- [21] Lorenzo Valbusa Dall’Armi, Angelo Ricciardone, and Daniele Bertacca. The Dipole of the Astrophysical Gravitational-Wave Background. *Journal of Cosmology and Astroparticle Physics*, 2022(11):040, November 2022. arXiv:2206.02747 [astro-ph, physics:gr-qc].
- [22] Joseph D. Romano and Neil J. Cornish. Detection methods for stochastic gravitational-wave backgrounds: a unified treatment. *Living Reviews in Relativity*, 20(1):2, April 2017.
- [23] Nicola Bartolo, Daniele Bertacca, Robert Caldwell, et al. Probing anisotropies of the Stochastic Gravitational Wave Background with LISA. *Journal of Cosmology and Astroparticle Physics*, 2022(11):009, November 2022. Publisher: IOP Publishing.
- [24] LISA Cosmology Working Group, Carlo R. Contaldi, Mauro Pieroni, et al. Maximum likelihood map making with the Laser Interferometer Space Antenna. *Physical Review D*, 102(4):043502, August 2020. Publisher: American Physical Society.
- [25] Jean-Baptiste Bayle, Quentin Baghi, Arianna Renzini, and Maude Le Jeune. LISA GW Response, February 2023. Language: eng.
- [26] Jean-Baptiste Bayle, Aurélien Hees, Marc Lilley, and Christophe Le Poncin-Lafitte. LISA Orbits, April 2022. Language: eng.
- [27] Jean-Baptiste Bayle and Olaf Hartwig. Unified model for the LISA measurements and instrument simulations. *Physical Review D*, 107(8):083019, April 2023. Publisher: American Physical Society.
- [28] Jean-Baptiste Bayle, Olaf Hartwig, and Martin Staab. LISA Instrument, September 2023.
- [29] Martin Staab, Jean-Baptiste Bayle, and Olaf Hartwig. PyTDI, March 2023. Language: eng.
- [30] Olaf Hartwig, Jean-Baptiste Bayle, Martin Staab, et al. Time-delay interferometry without clock synchronization. *Physical Review D*, 105(12):122008, June 2022. Publisher: American Physical Society.
- [31] Sharan Banagiri, Alexander Criswell, Tommy Kuan, et al. Mapping the gravitational-wave sky with LISA: a Bayesian spherical harmonic approach. *Monthly Notices of the Royal Astronomical Society*, 507(4):5451–5462, November 2021.
- [32] Nicola Bartolo, Daniele Bertacca, Robert Caldwell, et al. Probing anisotropies of the stochastic gravitational wave background with LISA. *Journal of Cosmology and Astroparticle Physics*, 2022(11):009, nov 2022.
- [33] LISA Science Study Team. Science Requirement Document. Technical Report ESA-L3-EST-SCI-RS-001, 2018.
- [34] Xavier Siemens, Vuk Mandic, and Jolien Creighton. Gravitational-wave stochastic background from cosmic strings. *Phys. Rev. Lett.*, 98:111101, Mar 2007.
- [35] Chia-Feng Chang and Yanou Cui. Stochastic gravitational wave background from global cosmic strings. *Physics of the Dark Universe*, 29:100604, 2020.
- [36] Alexander C. Jenkins and Mairi Sakellariadou. Anisotropies in the stochastic gravitational-wave background: Formalism and the cosmic string case. *Phys. Rev. D*, 98:063509, Sep 2018.
- [37] Mairi Sakellariadou. Cosmic strings and cosmic superstrings. *Nuclear Physics B - Proceedings Supplements*, 192-193:68–90, jul 2009.
- [38] M B Hindmarsh and T W B Kibble. Cosmic strings. *Reports on Progress in Physics*, 58(5):477–562, may 1995.
- [39] Chiara Caprini, Mikael Chala, Glauber C. Dorsch, et al. Detecting gravitational waves from cosmological phase transitions with LISA: an update. *Journal of Cosmology and Astroparticle Physics*, 2020(03):024, March 2020.
- [40] Chiara Caprini, Mikael Chala, Glauber C. Dorsch, et al. Detecting gravitational waves from cosmological phase transitions with LISA: an update. *Journal of Cosmology and Astroparticle Physics*, 2020(03):024–024, mar 2020.
- [41] Kazunori Kohri and Takahiro Terada. Semianalytic calculation of gravitational wave spectrum nonlinearly induced from primordial curvature perturbations. *Physical Review D*, 97(12), June 2018.
- [42] Rong-Gen Cai, Chao Chen, and Chengjie Fu. Primordial black holes and stochastic gravitational wave background from inflation with a noncanonical spectator field. *Physical Review D*, 104(8), oct 2021.
- [43] Bernard Carr, Florian Kühnel, and Marit Sandstad. Primordial black holes as dark matter. *Physical Review D*, 94(8), oct 2016.
- [44] Bernard Carr and Florian Kühnel. Primordial black holes as dark matter: Recent developments. *Annual Review of Nuclear and Particle Science*, 70(1):355–394, oct 2020.
- [45] Bruce Allen and Adrian C. Ottewill. Detection of Anisotropies in the Gravitational-Wave Stochastic Background. *Physical Review D*, 56(2):545–563, July 1997. arXiv: gr-qc/9607068.
- [46] S. Sinharay. Continuous probability distributions. In Penelope Peterson, Eva Baker, and Barry McGaw, editors, *International Encyclopedia of Education (Third Edition)*, pages 98–102. Elsevier, Oxford, third edition edition, 2010.
- [47] Gerhard Heinzel, Albrecht Rüdiger, and Roland Schilling. Spectrum and spectral density estimation by the Discrete Fourier transform (DFT), including a comprehensive list of window functions and some new at-top windows. 2002.
- [48] J. R. Bond, A. H. Jaffe, and L. Knox. Estimating the Power Spectrum of the Cosmic Microwave Background. *Physical Review D*, 57(4):2117–2137, February 1998. arXiv:astro-ph/9708203.
- [49] Daniel Foreman-Mackey, David W. Hogg, Dustin Lang, and Jonathan Goodman. emcee: The MCMC Hammer. *Publications of the Astronomical Society of the Pacific*, 125(925):306–312, March 2013. arXiv: 1202.3665.
- [50] Jonathan Goodman and Jonathan Weare. Ensemble samplers with affine invariance. *Communications in Applied Mathematics and Computational Science*, 5(1):65–80, January 2010. Publisher: Mathematical Sciences Publishers.

[51] Martin White, Lawrence M. Krauss, and Joseph Silk. Cosmic variance in cosmic microwave background

anisotropies: From 1 degrees to cobe. *The Astrophysical Journal*, 418:535, December 1993.